Modeling of Casting, Welding and Advanced Solidification Processes - XI
Edited by Charles-André Gandin and Michel Bellet
TMS (The Minerals, Metals & Materials Society), 2006

MODELING OF POROSITY FORMATION IN ALUMINUM ALLOYS

Kent D. Carlson[1], Zhiping Lin[1], Christoph Beckermann[1],
George Mazurkevich[2], and Marc C. Schneider[2]

[1] Dep. Mechanical and Industrial Engineering, University of Iowa, Iowa City, Iowa 52242, USA
[2] MAGMA Giessereitechnologie GmbH, Kackertstrasse 11, D-52072 Aachen, Germany

Keywords: porosity, aluminum alloys, hydrogen diffusion

Abstract

A new approach based on microsegregation of gas dissolved in the melt is used to model pore formation during the solidification of aluminum alloys. The model predicts the amount and size of the porosity in a solidified casting. Computation of the micro-/macro-scale gas species transport in the melt is coupled with the simulation of the feeding flow and calculation of the pressure field. The rate of pore growth is calculated based on the local level of gas supersaturation in the melt. The effect of the microstructure on pore formation is also taken into account. Parametric studies for one-dimensional solidification under an imposed temperature gradient and cooling rate illustrate that the model captures important phenomena observed in porosity formation in aluminum alloys. Comparisons between predicted porosity percentages and previous experimental measurements show good correspondence.

Introduction

Porosity-related defects are a major cause of casting rejection and re-work in the casting industry. Porosity formation has been investigated by many researchers, dating back to the early 1-D microporosity modeling work of Piwonka and Flemings [1], and the seminal 2-D work of Kubo and Pehlke [2]. An extensive review of the research progress in microporosity modeling, from these early studies up to work done in 2000, is provided by Lee et al. [3]. Recent examples of porosity models for aluminum alloy castings, including the effect of dissolved hydrogen, can be found in Sabau and Viswanathan [4] and Pequet et al. [5]. All of these models assume the local diffusion of hydrogen in the melt to be infinitely fast. In a series of experimental and theoretical studies, Lee and coworkers [6-10] have shown that diffusion of hydrogen through the supersaturated liquid (inside the mushy zone) to the pore can be a rate-controlling factor in pore growth for aluminum alloys. Lee and Hunt [6,7] experimentally observed porosity formation in aluminum alloys using an X-ray temperature gradient stage. They found the pressure drop caused by shrinkage to be negligibly small. They developed a model of hydrogen diffusion-controlled growth by considering a single pore inside the mushy zone. The model does not compute the pressure field in the mushy zone; rather, the pressure is an input variable. Atwood et al. [8,9] applied this model to an Al7Si alloy, and Hamilton et al. [10] incorporated it into a heat flow model for complex-shaped castings, still neglecting pressure variations.

The present study of porosity formation in aluminum alloys focuses on incorporating into the porosity model of Carlson et al. [11] a model for local, finite-rate gas species diffusion through the liquid metal to the pores. As in Ref. [11], the pressure field and feeding flows in the liquid

metal as well as in the mushy zone are determined using a single-domain approach. The model is tested for one-dimensional, directional solidification of the (un-modified) alloy A356 with a constant temperature gradient and cooling rate. The results are compared to measurements available in the literature. The importance of accounting for finite-rate diffusion of hydrogen to the pores is demonstrated.

Model Description

The present multi-phase model assumes that each volume element in the casting is composed of some combination of solid metal (*s*), liquid metal (*l*) and porosity (*p*), such that the volume fractions satisfy $\varepsilon_s + \varepsilon_l + \varepsilon_p = 1$. Mixture properties are obtained as the sum of the property values for each phase multiplied by their respective volume fractions. For example, the mixture density is given by: $\rho = \varepsilon_s \rho_s + \varepsilon_l \rho_l + \varepsilon_p \rho_p$. For the purpose of the parametric studies presented below, the temperature field is prescribed. The solid fraction (ε_s) is assumed to be known from solidification path data as a function of temperature.

Mixture Mass Conservation. The mixture continuity equation is simplified by assuming that the solid metal and the porosity are stationary. The continuity equation is then given by [11]

$$\frac{\partial}{\partial t}\left(\varepsilon_s \rho_s + \varepsilon_l \rho_l + \varepsilon_p \rho_p\right) + \nabla \cdot \left(\rho_l \mathbf{v}\right) = 0 \tag{1}$$

or

$$\nabla \cdot \mathbf{v} = -\frac{1}{\rho_l}\left[\frac{\partial}{\partial t}\left[\varepsilon_s\left(\rho_s - \rho_l\right) + \rho_l - \varepsilon_p\left(\rho_l - \rho_p\right)\right] + \mathbf{v} \cdot \nabla \rho_l\right] = CRHS \tag{2}$$

where $\mathbf{v}$ denotes the superficial liquid velocity, $\mathbf{v} = \varepsilon_l \mathbf{v}_l$. Eq. (2) shows that the divergence of the velocity field is a function of the solidification contraction, liquid density change, porosity evolution, and gradients in the liquid density (although this last contribution is small).

Liquid Momentum Conservation. The melt velocity, **v**, is determined from [11]

$$\nabla^2 \mathbf{v} = \frac{\varepsilon_l}{K}\mathbf{v} + \frac{\varepsilon_l}{\mu_l}\nabla P - \frac{\varepsilon_l}{\mu_l}\rho_{ref}\mathbf{g} \tag{3}$$

where *P* is the melt pressure, **g** is the gravity vector, ρ_{ref} is a reference liquid density, taken as the melt density at the liquidus temperature, and μ_l is the dynamic viscosity of the liquid, which is assumed constant and taken as the melt value at the liquidus temperature. Buoyancy-induced flow is neglected. The permeability, K, is given by $K = K_0\, \varepsilon_l^3 / \left(1 - \varepsilon_l\right)^2$, where $K_0 = \lambda_2^2 / 180$, in which λ_2 is the secondary dendrite arm spacing (SDAS). The SDAS is given by $\lambda_2 = \left[\lambda_{2,0}^3 + M\left(t - t_L\right)\right]^{1/3}$, where $\lambda_{2,0}$ is an initial spacing (estimated as 20 μm in the present study), M is a coarsening constant (estimated as $M = 2600$ μm^3/s from experimental Al-7Si data [12]), and $\left(t - t_L\right)$ is the time (in seconds) elapsed since solidification began. The inertial terms have been neglected in the momentum equation. Notice that Eq. (3) reduces to Stokes' equation in the single-phase liquid region, where *K* becomes very large. In the mushy zone, the left-hand side of Eq. (3) becomes very small relative to the permeability term, and the equation then reduces to Darcy's law.

Melt Pressure. By manipulating and combining Eq. (2) and Eq. (3), it is possible [11] to derive the following equation for the melt pressure, *P*:

$$\nabla\cdot\left(\frac{K}{\mu_l}\nabla P\right)=-(CRHS)+\nabla\cdot\left(\frac{K}{\mu_l}\rho_{ref}\mathbf{g}\right)+\nabla\cdot\left(\frac{K}{\varepsilon_l}\nabla^2\mathbf{v}\right) \tag{4}$$

where $CRHS$ is the right-hand side of Eq. (2).

Gas Species Conservation. The average concentration of hydrogen dissolved in the melt, C_l (in wt fraction), is obtained from the mixture species conservation equation [11]

$$\frac{\partial}{\partial t}\left(\varepsilon_s\rho_s C_s+\varepsilon_l\rho_l C_l+\varepsilon_p\rho_p C_p\right)+\nabla\cdot\left(\rho_l C_l\mathbf{v}\right)=0 \tag{5}$$

For fast diffusion in the solid, the concentration of hydrogen in the solid is approximately given by $C_s=\kappa_{sl}C_l$, where κ_{sl} is the partition coefficient of hydrogen between the solid and the liquid. Since the porosity is composed of hydrogen only, the hydrogen concentration in the pores is unity (i.e., $C_p=1$).

Pore Size. An effective pore radius is calculated as in Pequet et al. [5] from

$$r_p=\mathrm{MAX}\left[r_0;\mathrm{MIN}\left(r_{sphere};r_{dend}\right)\right] \tag{6}$$

where r_0 is a negligibly small initial pore radius (taken as 1 μm), $r_{sphere}=\left[3\varepsilon_p/(4\pi n)\right]^{1/3}$, in which n is the pore number density, and $r_{dend}=\lambda_2(1-\varepsilon_s)/(2\varepsilon_s)$. In the equation for r_{dend}, ε_s is held constant once the eutectic starts to form; also, r_{dend} is held constant once $r_p=r_{dend}$. In the latter case, the pores continue to grow between the dendrite arms by assuming an ellipsoidal shape; once the length of the (ellipsoidal) pores exceeds the distance between the pores ($\approx n^{-1/3}$), the pores are assumed to merge (creating so-called "connected" porosity).

Gas Microsegregation. The gas microsegregation equation is derived by combining the gas species conservation equation for the pore phase with the gas species balance at the interface between the pore and liquid phases - the details of the derivation will be presented elsewhere. With $C_p=1$, the result can be written as:

$$\frac{\partial}{\partial t}\left(\varepsilon_p\rho_p\right)=\frac{S_{lp}\rho_l D_l}{l_{lp}}\frac{\left(C_l-C_{lp}\right)}{1-C_{lp}}=\gamma_{lp}\Omega_l \tag{7}$$

where C_{lp} is the equilibrium concentration of hydrogen in the liquid at the pore/liquid interface (in wt fraction), S_{lp} is the interfacial area concentration of the pores (pore surface area per unit volume), D_l is the mass diffusivity of hydrogen in the melt, and l_{lp} is a liquid diffusion length at the pore/liquid interface. The second equality in Eq. (7) defines a growth factor $\gamma_{lp}=S_{lp}\rho_l D_l/l_{lp}$ and a normalized liquid supersaturation $\Omega_l=\left(C_l-C_{lp}\right)/\left(1-C_{lp}\right)$. The interfacial area concentration is approximated in the present study as $S_{lp}=4\pi n r_p^2\phi$, where ϕ is an impingement factor taken as $1-\varepsilon_s$. The diffusion length is simply calculated from $l_{lp}=r_p$, which is based on the well-known analytical result for the species boundary layer thickness around a sphere. Figure 1 illustrates the concept of the species diffusion length. For a finite supersaturation in the melt, when the average gas species concentration C_l is larger than the equilibrium concentration at the pore/liquid interface C_{lp}, hydrogen diffuses towards the pore and the pore grows (i.e., ε_p increases). For large γ_{lp}, which occurs for a large interfacial area (e.g., with a high pore density, *n*) and/or a small diffusion length, the melt becomes well-mixed

(C_l tends to C_{lp}), since the pore growth rate $\partial(\varepsilon_p \rho_p)/\partial t$ must be finite. Note from Eq. (7) that the pore volume fraction, ε_p, also changes in response to changes in the pore density, ρ_p. The pore density is calculated from the ideal gas law, $\rho_p = P_p/(RT)$, where P_p is the pore pressure, R is the gas constant for hydrogen, and T is the absolute temperature. In the present model, Eq. (7) is actually solved for the equilibrium concentration at the liquid/pore interface, C_{lp}. As in Ref. [11], the pore volume fraction ε_p is then determined from the continuity equation, Eq. (1). Hence, the effects of feeding flows and solidification shrinkage (and other density changes) on ε_p are still taken into account.

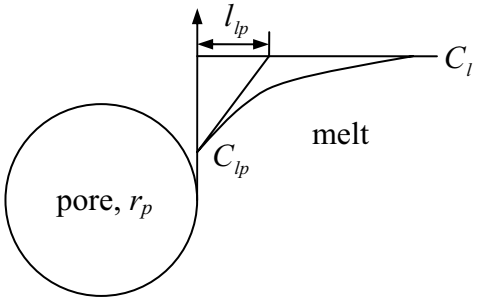

Figure 1. Hydrogen diffusion boundary layer around a growing pore.

Pore Pressure. The pore pressure is calculated from Sievert's law

$$P_p = \left[100\, C_{lp}\left(\frac{f}{K_e}\right)\right]^2 \times 101{,}325 \tag{8}$$

where the value 100 converts C_l from wt fraction to wt pct, and the value 101,325 converts the pressure from atm to Pa. When no pores are present, C_l is used in place of C_{lp}. In Eq. (8), f and K_e are the activity and equilibrium coefficients of the hydrogen gas species, respectively. The equilibrium coefficient is a function of temperature, given by $\log_{10} K_e = -a/T - b$, where a and b are coefficients. The activity coefficient is given as a function of the silicon and copper concentrations in the melt by $\log_{10} f = e_H^{Si} C_l^{Si} + r_H^{Si}\left(C_l^{Si}\right)^2 + e_H^{Cu} C_l^{Cu} + r_H^{Cu}\left(C_l^{Cu}\right)^2$, where e_H and r_H are interaction coefficients, and C_l^{Si} and C_l^{Cu} are the concentrations (in wt pct) of silicon and copper in the melt. Until the eutectic forms, these concentrations are approximately given by the Scheil equation as $C_l^{Si} = C_0^{Si}\left(1-\varepsilon_s\right)^{\kappa^{Si}-1}$ and $C_l^{Cu} = C_0^{Cu}\left(1-\varepsilon_s\right)^{\kappa^{Cu}-1}$, respectively, where C_0^{Si} and C_0^{Cu} are the initial concentrations of these elements and κ^{Si} and κ^{Cu} are the partition coefficients for silicon and copper in the aluminum alloy. During and after the eutectic formation, the activity coefficient is held constant.

Capillary Pressure. The capillary pressure is modeled as

$$P_\sigma = \frac{2\sigma}{\mathrm{MAX}(r_p; r_{nuc})} \tag{9}$$

where σ is the surface tension. The effective pore radius at nucleation, r_{nuc}, may be calculated from $r_{nuc} = r_0/\Phi$, where Φ is a heterogeneous nucleation parameter (less than unity). However, neither the initial pore radius nor the heterogeneous nucleation parameter are known to any degree of accuracy. Furthermore, pores may not actually nucleate in the melt, but can evolve from small gas pockets inside entrained oxide films. Therefore, r_{nuc} is simply used in the present study as a parameter to control the *maximum* capillary pressure at which the pores nucleate or start to grow. Once $r_p > r_{nuc}$, Eq. (9) gives the capillary pressure corresponding to a pore of radius r_p.

Porosity Formation. Porosity is assumed to nucleate if $P \le P_p - P_\sigma$. When porosity forms, the melt pressure at that location is forced to $P = P_p - P_\sigma$ [11].

Results

Numerical simulations were conducted for directional solidification of the aluminum alloy A356. Due to space limitations, it is not possible to list all of the thermophysical properties used in the simulations. Suffice it to say that they were collected from Refs. [5,9,12-16]. The system domain is one-dimensional (in x) with a zero flow boundary condition at the left ($x = 0$) side and atmospheric pressure applied at the right (inflow) boundary. A linear temperature profile is translated across the domain with a speed given by $\dot{T}/G$, where $\dot{T}$ is the cooling rate. The temperature gradient, G, is held constant at a value typical of previous experiments (see below), i.e., $G = 500$ K/m; it can be shown that the results do not strongly depend on G. The simulations are started in the fully liquid state and continued until steady growth is reached.

Figure 2 shows profiles of some of the calculated dependent variables for an initial hydrogen level in the melt of $C_0 = 0.13$ cc/100g and a cooling rate of 0.5°C/s. The pore density in this simulation is 10^9 m^{-3}, and the maximum capillary pressure, $P_{\sigma,nuc} = 2\sigma/r_{nuc}$, is 1.6 bar, which corresponds to $r_{nuc} \approx 10$ μm. The temperature increases linearly in the positive x-direction. Results are shown at a time in the simulation when there is a fully solidified layer next to $x = 0$. Figure 2a indicates that the porosity starts to form at the beginning of the eutectic reaction (when the liquid fraction, ε_l, is about 35%). The pore fraction continues to increase until the melt is completely solidified. The melt pressure drop is very small until the eutectic reaction; subsequently, the melt pressure P decreases more significantly, due to the permeability decreasing strongly as the liquid fraction approaches zero. The pore pressure, P_p ($= P + P_\sigma$), during pore growth reflects this decrease. The P_p profile before pore formation illustrates the increase in the equilibrium gas pressure with decreasing temperature according to Sievert's law. Note that the capillary pressure, P_σ, rapidly reduces from the initial value of $P_{\sigma,nuc} = 1.6$ bar to about 0.9 bar due to the increase in the pore radius, r_p, during the initial pore growth stage; subsequently, P_σ remains constant at 0.9 bar, because r_p is limited by the dendritic network (r_{dend}). Figure 2b illustrates the development of the hydrogen supersaturation in the melt. Before porosity formation, the average hydrogen concentration in the melt, C_l, increases with decreasing temperature because of rejection (partitioning) of hydrogen from the growing solid; the equilibrium concentration, C_{lp}, from Sievert's law decreases primarily because of the decreasing temperature. At the point where porosity starts to form, $C_l = C_{lp}$. Then, the concentration C_l rapidly increases due to the high rate of solidification during eutectic formation, while C_{lp} continues to decrease. The difference $C_l - C_{lp}$ in Fig. 2b reflects the significant level of hydrogen supersaturation in the melt during pore growth. Also note that the growth factor γ_{lp} varies considerably during pore formation.

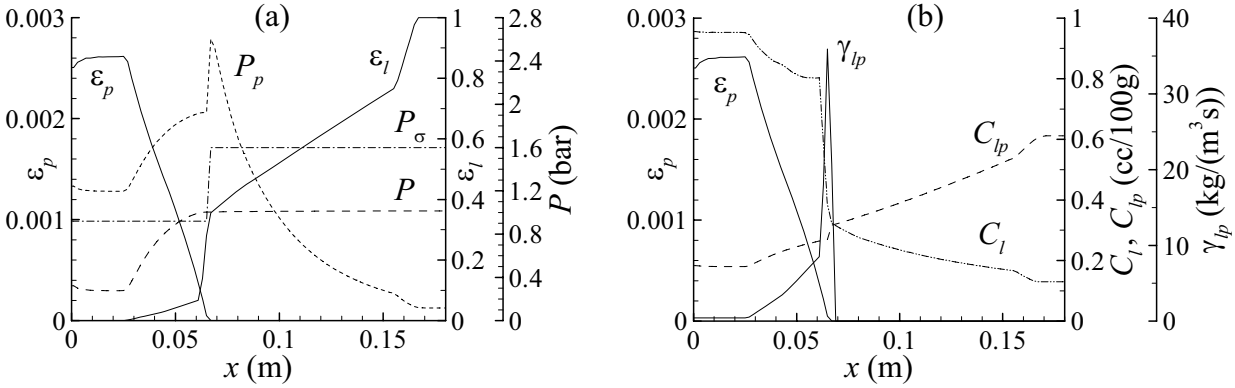

Figure 2. Profiles of computed variables during directional solidification of A356.

Before exploring the effect of finite-rate diffusion of hydrogen in the liquid in more detail, it is important to better understand the role of the maximum capillary pressure at the beginning of pore growth, $P_{\sigma,nuc}$, on porosity formation. Thus, a number of simulations were performed where the growth factor, γ_{lp}, was set to a very large value, thus modeling complete (infinitely fast) local diffusion of hydrogen in the melt. The results, shown in Fig. 3, correspond to $\dot{T} = 1$ ºC/s and $n = 10^{11}$ pores/m^3. In Fig. 3a, the calculated final pore volume percentage (at steady state) is plotted as a function of the initial hydrogen content, C_0, for $P_{\sigma,nuc} = 0$, 1.6, and 16 bar. For $P_{\sigma,nuc} = 0$, ε_p increases almost linearly with increasing C_0; the small but finite ε_p near $C_0 = 0$ is the remaining shrinkage porosity. At a given gas level, the porosity levels are significantly lower for the two finite $P_{\sigma,nuc}$. Interestingly, the predicted ε_p are quite similar for $P_{\sigma,nuc} = 1.6$ and 16 bar, other than that a more pronounced "threshold" hydrogen level, below which $\varepsilon_p \approx 0$, can be observed for $P_{\sigma,nuc} = 16$ bar. This indicates that for reasonably large $P_{\sigma,nuc}$ (e.g., greater than ~1 bar), the capillarity effect ceases to have an important influence on the final porosity levels, other than for low hydrogen contents. However, as shown in Fig. 3b, increasing $P_{\sigma,nuc}$ continues to have an effect on the solid fraction at which porosity first forms. As higher the maximum capillary pressure, the later during solidification porosity nucleates. Note that $P_{\sigma,nuc} = 1.6$ bar is a physically reasonable value, whereas 16 bar is much too high. Figure 3b also shows that for high hydrogen contents (and $P_{\sigma,nuc} = 1.6$ bar), porosity can nucleate at very low solid fractions, well before any eutectic starts to form.

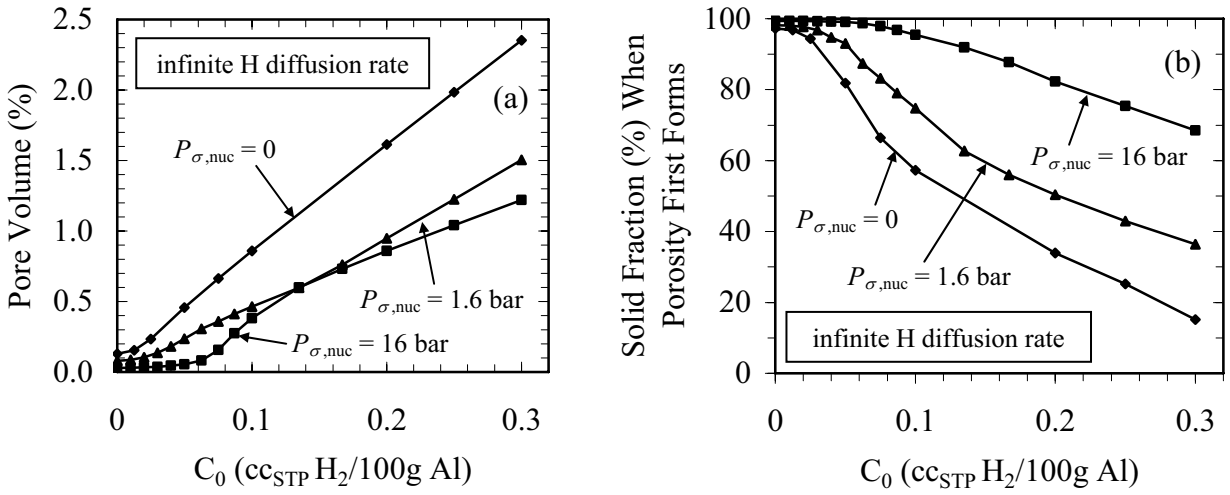

Figure 3. Variation of (a) final pore volume and (b) solid fraction at pore formation with C_0.

The effect of finite-rate diffusion of hydrogen in the liquid on pore formation, as modeled by Eq. (7), is explored in Fig. 4. The initial hydrogen content is fixed at $C_0 = 0.13$ cc$_{STP}$$H_2$/100g Al, and $P_{\sigma,nuc}$ is taken as 1.6 bar. In Fig. 4, the calculated final pore volume percentages (solid symbols connected by lines) are plotted against the cooling rate, $\dot{T}$. The cooling rate is the single most important parameter in porosity formation, because it determines the extent of finite-rate diffusion of hydrogen in the liquid as well as the velocity of the feeding flow and, hence, the magnitude of the liquid pressure drop in the mushy zone. The results of three sets of simulations are shown: (1) $\gamma_{lp} \to \infty$ (infinitely fast diffusion) and $n = 10^{11}$ m^{-3}; (2) γ_{lp} finite and $n = 10^{11}$ m^{-3}; and (3) γ_{lp} finite and $n = 10^{9}$ m^{-3}. The number density of pores is varied in Cases 2 and 3, because the magnitude of the growth factor γ_{lp} in Eq. (7) depends strongly on n: the higher the pore number density, the higher the interfacial area per unit volume (i.e., $\gamma_{lp} \sim S_{lp} \sim n$). Physically, a higher growth factor leads to more complete diffusion of hydrogen in the liquid.

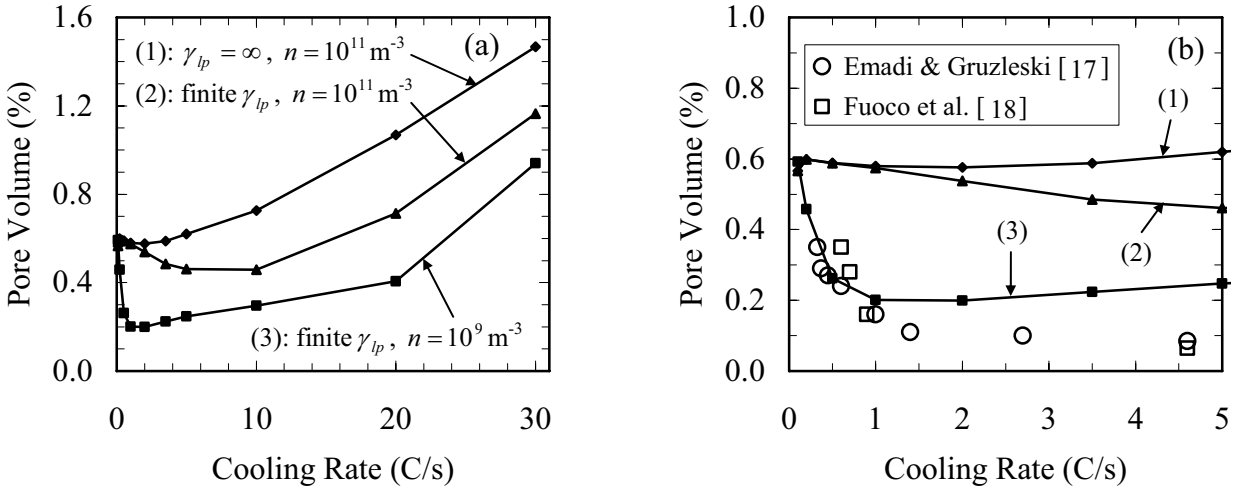

Figure 4. Variation of pore volume percentage with cooling rate, showing (a) cooling rates up to 30ºC/s, and (b) a magnified view of the lower cooling rates, with experimental data.

Focusing first on Case 1 (infinitely fast local diffusion of hydrogen in the liquid), it can be seen from Fig. 4 that the pore volume percentage generally increases with increasing cooling rate, except for a small dip for $\dot{T}$ below 5°C/s (Fig. 4b). This can be explained by the liquid pressure drop increasing, since a higher cooling rate causes (i) higher feeding velocities and (ii) smaller secondary dendrite arm spacings which, in turn, reduce the permeability. This is the same effect that is reflected by the well-known Niyama criterion, which is a thermal parameter given by the ratio $G/\sqrt{\dot{T}}$. It has been shown for steel castings that the porosity increases with a decreasing Niyama criterion value (and, hence, an increasing cooling rate) [19]. In solidification of A356 with a moderate hydrogen level, this effect comes into play only at high cooling rates (i.e., $\dot{T} > 5-10$ °C/s), because of the large fraction of eutectic. As noted in connection with Fig. 2, the liquid pressure drop is generally small up to the point where the eutectic starts to form.

For the two cases with a finite growth factor γ_{lp} (Cases 2 and 3), Fig. 4 shows that, for a given cooling rate, the calculated pore volume percentages are significantly lower than in Case 1. This illustrates the reduction in the pore growth rate due to finite-rate diffusion of hydrogen in the melt [see Eq. (7)]. Only as the cooling rate tends to zero (very long solidification times) do the predictions for the three cases approach each other; this can be explained by the long time available for diffusion. As expected from Eq. (7), the pore volume percentages are lower for $n = 10^9$ m^{-3} (Case 3) than for 10^{11} m^{-3} (Case 2). However, all three cases show the previously observed increase in ε_p with $\dot{T}$ for cooling rates above about $5-10$ °C. As can be seen from Fig. 4b, the pore volume percentages calculated for Case 3 ($n = 10^9$ m^{-3}) show the same steep decrease with increasing cooling rate up to about 1°C/s as measured in previous experiments [17,18]. This comparison lends some confidence into the present model, since such a decrease in ε_p does not appear to be possible without accounting for finite-rate diffusion of hydrogen in the liquid. Above a cooling rate of 1°C/s, the experimental data for ε_p are somewhat below the predictions for Case 3. This disagreement could be attributed to a number of factors, including the neglect of the solidification path dependence on the cooling rate (which can be very important for high cooling rates), uncertainties in the permeability relation and the calculation of the secondary dendrite arm spacing, an over-simplified model for the diffusion length l_{lp}, and the fact that the number density of pores can depend on the cooling rate. Only comparisons with experimental data at very high cooling rates (e.g., 30°C/s) could clarify these remaining uncertainties in the model.

Conclusions

A gas microsegregation model has been developed for porosity formation in aluminum alloys. By incorporating the effect of local, finite-rate diffusion of dissolved hydrogen in the liquid into an existing porosity model [11], the effects of feeding flow and melt pressure are taken into account as well. The comparisons with previous experimental measurements conclusively show that pore growth can indeed be limited by finite-rate diffusion of hydrogen. Additional study is needed to fine-tune the model for high cooling rates and to clarify the effect of melt modification (e.g., Sr addition to the aluminum alloy). The model is general in that it can be immediately applied to fully three-dimensional casting situations, as demonstrated in Ref. [11] without gas microsegregation.

References

1. T.S. Piwonka and M.C. Flemings, *Trans. AIME*, 236 (1966), 1157-1165.

2. K. Kubo and R.D. Pehlke, *Metall. Trans. B*, 16B (1985), 359-366.

3. P.D. Lee, A. Chirazi, and D. See, *J. Light Metals*, 1 (2001), 15-30.

4. A.S. Sabau and S. Viswanathan, *Metall. Mater. Trans. B*, 33B (2002), 243-255.

5. Ch. Pequet., M. Gremaud, and M. Rappaz, *Metall. Mater. Trans. A*, 33A (2002), 2095-2106.

6. P.D. Lee and J.D. Hunt, *Modeling of Casting, Welding and Advanced Solidification Processes VII*, ed. M. Cross and J. Campbell (Warrendale, PA: TMS, 1995), 585-592.

7. P.D. Lee and J.D. Hunt, *Acta Mater.*, 45 (1997), 4155-4169.

8. R.C. Atwood, S.Sridhar, W. Zhang and P.D. Lee, *Acta Mater.*, 48 (2000), 405-417.

9. R.C. Atwood and P.D. Lee, *Metall. Mater. Trans. B*, 33B (2002), 209-221.

10. R.W. Hamilton, D. See, S. Butler, and P.D. Lee, *Mat. Sci. Eng.*, A343 (2003), 290-300.

11. K.D. Carlson, Z. Lin, R.A. Hardin, C. Beckermann, G. Mazurkevich, and M.C. Schneider, *Modeling of Casting, Welding and Advanced Solidification Processes X*, ed. D.M. Stefanescu et al. (Warrendale, PA: TMS, 2003), 295-302.

12. S. Shivkumar, D. Apelian, J. Zou, *AFS Trans.*, 98 (1990), 897-904.

13. *MAGMASOFT*, MAGMA GmbH, Kackerstrasse 11, 52072 Aachen, Germany.

14. G.K. Sigworth and T.A. Engh, *Metall. Trans. B*, 13B (1982), 447-460.

15. D. Emadi, J.E. Gruzleski and J.M. Toguri, *Metall. Trans. B*, 24B (1993), 1055.

16. G.K. Sigworth and C. Wang, *AFS Trans.*, 100 (1992), 989-1004.

17. D. Emadi and J.E. Gruzleski, *AFS Trans.*, 102 (1994), 307-312.

18. R. Fuoco, H. Goldenstein and J.E. Gruzleski, *AFS Trans.*, 102 (1994), 297-306.

19. K.D. Carlson, S. Ou, R.A. Hardin, and C. Beckermann, *Metall. Mater. Trans. B*, 33B (2002) 731-740.